Structure, Thermodynamics, and Dynamics of Thin Brine Films in Oil-Brine-Rock Systems

Chao Fang,[1] Shuyu Sun,[2] Rui Qiao[1,*]

[1] Department of Mechanical Engineering, Virginia Tech, Blacksburg, VA 24061
[2] Division of Physical Science and Engineering, King Abdullah University of Science and Technology, Thuwal 23955-6900, Saudi Arabia

ABSTRACT: Thin brine films are ubiquitous in oil-brine-rock systems such as oil reservoirs and play a crucial role in applications such as enhanced oil recovery. We report the results of molecular simulations of brine films that are confined between model oil (*n*-decane) and rock (neutral or negatively charged quartz slabs), with a focus on their structure, electrical double layers, disjoining pressure, and dynamics. As brine films are squeezed to ~0.7 nm (~3 water molecule layers), the structures of the water-rock and water-oil interfaces change only marginally, except that the oil surface above the brine film becomes less diffuse. As the film is thinned from ~1.0 to ~0.7 nm, ions are enriched (depleted) near the rock (oil) surface, especially at a bath ion concentration of 0.1 M. These changes are caused primarily by the reduced dielectric screening of water and the weakened ion hydration near water-oil interfaces and, to a smaller extent, by the increased confinement. When the brine film is ~1.0-nm thick, hydration and EDL forces contribute to the disjoining pressure between the charged rock and the oil. The EDL forces are reduced substantially as the ion concentration increases from 0.1 to 1.0 M and the magnitude of the reduction is close to that predicted by the Poisson-Boltzmann equation. When the brine film is thinned from ~1.0 to ~0.7 nm, the disjoining pressure increases by ~10 MPa, which is mostly due to an increase in the hydration forces. The first layer of water on the rock surface is nearly stagnant, even in 0.74-nm-thick brine films, whereas the viscosity of water beyond the first layer is bulk-like and the slip coefficient of oil-water interfaces is close to that under unconfined conditions. The insights that are obtained here help lay a foundation for the rational application of technologies such as low-salinity waterflooding.

* Corresponding author. Email: ruiqiao@vt.edu.

1. Introduction

Thin liquid films that are confined between surfaces are ubiquitous in nature and engineering systems, e.g., in colloids, foams, nanofluidic chips, desalination membranes that are based on layered materials, and porous electrodes of supercapacitors.[1-4] The diverse chemistry of the confining surfaces and liquids, together with the confinement that is imposed by surfaces, endow thin liquid films with rich structures at molecular and mesoscopic scales. For example, water forms distinct layers with enhanced density near rigid, hydrophilic surfaces but depletion layers with reduced density near soft, hydrophobic surfaces.[5-8] When the confining surfaces carry net charges, an electrical double layer (EDL) emerges in the liquid film and the EDL's structure depends strongly on the characteristics of the liquid (e.g., solvent-free ionic liquids vs. dilute aqueous solutions), the concentration of bulk ions, and the thicknesses of the films, among other factors. Thin liquid films often exhibit dynamic properties that differ from those of bulk liquids and fascinating thermodynamics. The latter can manifest as the surface forces they mediate, the phase behaviors they display, and the charges they store. Liquid films can mediate a host of surface forces with vastly different ranges and strengths, e.g., the steric force, hydration force, hydrophobic force, double-layer force, and van der Waals force. The structure, dynamics, and thermodynamics of thin liquid films play an essential role in numerous problems, e.g., the stability of colloids and foams, boundary lubrication, throughput of desalination by graphene-derived membranes, to name just a few.[9-13] As such, thin liquid films have been studied extensively via experimental, theoretical, and simulation approaches.[10, 14-15]

In petroleum reservoirs, which are essentially oil-brine-rock (OBR) systems, thin brine films are often found between rocks and oil droplets.[16-17] The thicknesses of these films depend on the characteristics of the rock surfaces, the brine composition, and the properties of the oil droplets and can range from a few angstroms to tens of nanometers.[18-19] For example, using small-angle neutron scattering, it was demonstrated that water films with a thickness of ~0.8-1.3 nm exist on the surfaces of silica particles that are dispersed in heptane using anionic surfactants.[19] Despite their small thickness, brine films can play a fundamental role in oil recovery from reservoirs. For example, the contact angle of oil droplets on rock surfaces, which is a primary factor that governs the recovery of oil,[20] depends strongly on the disjoining pressure in these films.[17, 21] Indeed, some enhanced oil recovery (EOR) techniques are posited to function via the modification of thin brine

films in OBR systems. For example, in low-salinity waterflooding (LSW), water with low salt concentration is injected into reservoirs and notable success has been reported in many field studies.[22-27] While multiple mechanisms are likely responsible for EOR, an emerging consensus is that the expansion of EDLs in the brine films that is caused by the decrease of brine's ion concentration and the ensuing increase of the EDL disjoining pressure in the films play a key role by making the rock surface more water-wet.[16, 21] In addition to their structure and disjoining pressure, which affect the thermodynamics of EOR, the dynamics of brine films are expected to play a key role in determining the kinetics of LSW.[28-29]

Insights into the structure, thermodynamics, and dynamics of brine films in OBR systems may facilitate the improvement of existing EOR techniques and/or the formulation of new EOR concepts. While such insights may be derived from prior works on thin liquid films in other systems, the unique properties of OBR systems can render this approach difficult. For example, the brine films in some OBR systems can have subnanometer thickness.[19] These brine films exhibit two interesting features: First, these brine films are confined by a solid rock with a rigid surface and an oil phase with a soft, diffusive surface. Second, the thickness of these brine films is comparable to key intrinsic length scales of the brine solution, brine-rock interfaces, and brine-oil interfaces (e.g., the Debye length of brine, the hydration diameter of the ions in brine, the characteristic length of the density oscillation of water molecules near rock surfaces, and the width of diffuse brine-oil interfaces). The combination of these features renders these brine films highly unique; thus, it is difficult to extrapolate the insights that are obtained in the studies of other thin liquid films to them.

In principle, molecular dynamics (MD) simulations, in which the thin brine film, oil, and rock are resolved with atomistic resolution, can be used to gain insights into the molecularly thin brine films in OBR systems. Indeed, molecular simulations of OBR systems have been reported and insights such as effects of salinity on the wettability of oil on rock surface have been obtained.[30-36] However, the brine films in these studies, if they exist, are often bound by oil droplets or pores with a width of several nanometers. With this type of setup, the brine films typically extend less than 2 nm laterally and their thickness varies substantially in the lateral direction. Consequently, these studies do not address the scenario of extended brine films that is encountered in practice. Many questions on the structure, thermodynamics, and dynamics of extended brine films that are

found in practical OBR systems remain open. For example, what are the molecular structures of the rock-brine and brine-oil interfaces in these films and how do these interfaces evolve as the brine film approaches molecular thickness? How are ions distributed in the EDLs in the brine film and how does the ion distribution respond to changes in the bulk ion concentration and film thickness? What is the disjoining pressure inside these films? What is the relative contribution of the hydration and EDL forces to the total disjoining pressure? How do these forces change with the film thickness and bulk ion concentration?

In this work, we conduct extensive MD simulations to study extended brine films that are sandwiched between rock surfaces and thick slabs of oil. Our overarching objective is to clarify the structure, thermodynamic properties, and hydrodynamic properties of thin brine films that are relatively ideal but still relevant to practical OBR systems. In terms of structure, we seek to identify the molecular structures of the rock-brine and brine-oil interfaces in these films and their evolutions as the brine films approach molecular thickness. We also investigate the ion distribution in the EDLs in the brine films and its response to changes in the bulk ion concentration and film thickness. In terms of thermodynamic properties, we seek to determine the disjoining pressure in molecularly thin brine films and to investigate the relative contributions of the hydration and EDL forces to the total disjoining pressure. We also seek to quantify the effective dielectric properties of the brine films and how they change as the film thickness is reduced. In terms of hydrodynamic properties, we seek to quantify the effective viscosity of brine films and the possible slip at brine-oil interfaces. The remainder of the manuscript is organized as follows: In Section 2, the molecular systems and simulation methods are presented. In Section 3, the structure of brine films and the disjoining pressure in them are quantified at several film thickness and brine concentrations and the mechanisms that underlie the observed results are discussed. The hydrodynamic properties of the brine films are also presented. Finally, the conclusions of this work are presented in Section 4.

2. Materials and Methods

The molecular modeling of OBR systems is complicated by the diverse composition of oil, brine, and rock in oil reservoirs: the rocks can be sandstone or carbonate;[16] the brine can contain a variety of ions, e.g., Na^+, Cl^-, Ca^{2+}, and Mg^{2+}; and the oil is a mixture of many hydrocarbons, basic and acidic groups (e.g., naphtenic acids), and impurities. Since the molecular study of OBR system is highly limited at present, we focus on a simplified description of OBR here. Quartz slabs are

used as model rock because quartz is a key component of sandstone. Aqueous NaCl solution is used as the brine and pure *n*-decane is used as the oil. The surfaces of the quartz slabs that face brine and oil are negatively charged in most simulations to be consistent with experimental data at typical pH, although neutral surfaces are also considered as a reference (see below). The oil-brine interface is neutral, which corresponds to the limit of very low density of electroactive species at the water-oil interfaces.[37]

Simulation systems. Three types of systems have been simulated: The first type of system, namely, the "*thin brine film*" system, is used to study molecularly thin brine films that are confined between rock and oil surfaces. As shown in Fig. 1a, this type of system consists of a quartz slab, an oil reservoir, a brine reservoir and brine film, and two rigid pistons that bound the oil and brine reservoirs. The quartz slab is ~3 nm thick. Its surface that faces the brine film and oil has a surface charge density of –0.12 C/m^2. A brine film is formed between the upper rock surface and the oil phase and it is connected with the brine reservoir. Its thickness ranges from 0.7 to 1.0 nm, which is within the range of brine film thickness that was identified via neutron scattering.[16, 38] To maintain a bulk-like behavior at positions that are away from the rock surface, the initial brine and oil reservoirs measure ~5 nm and ~4 nm, respectively, in the *z*-direction. The top piston is used to control the thickness of the brine film (see below); the bottom piston is used to prevent water molecules from evaporating and it can move freely in the *z*-direction. The system is periodic in all directions; however, two large vacuum spaces are placed outside the pistons to effectively interrupt the periodicity in the *z*-direction. The simulation box measures 14.00×3.93×18.00 nm^3 in the *x*-, *y*-, and *z*-directions, respectively.

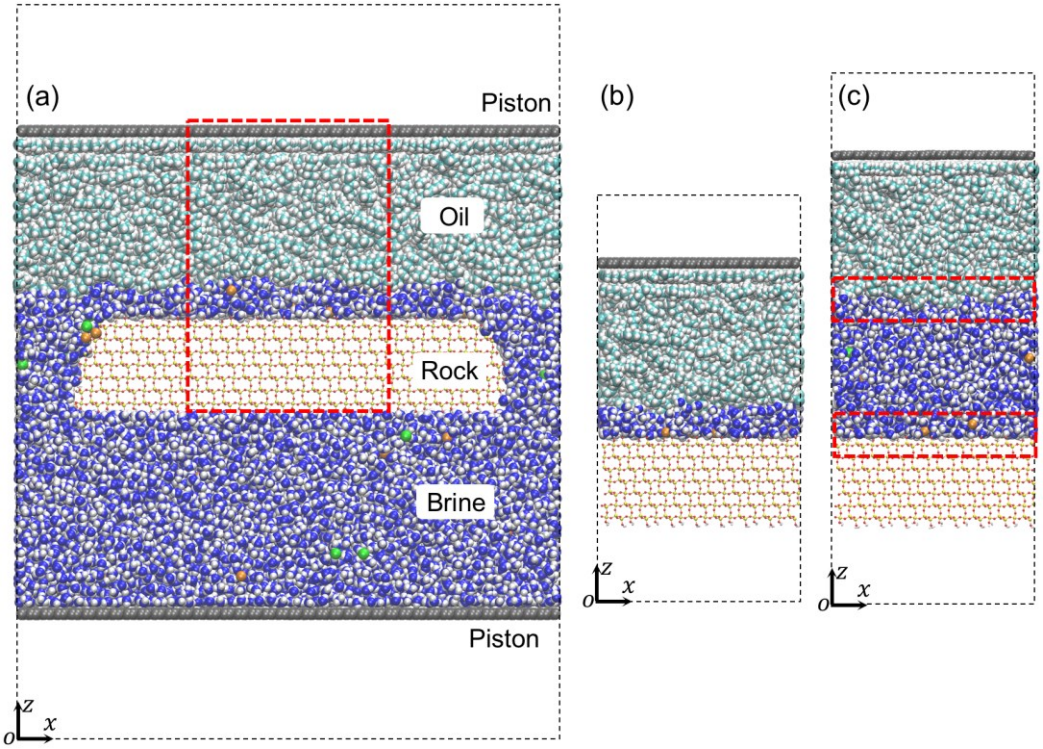

Figure 1. *The molecular systems for studying oil-brine-rock (OBR) systems.* **(a)** A snapshot of a model OBR system featuring a thin brine film, a brine reservoir, and a thick oil slab. The pressure in the brine reservoir and oil is regulated using two pistons. The black dashed box shows the simulation box. The 5.5 nm-wide red box denote the region in which the statistics of brine films are taken. **(b)** A snapshot of system for investigating the dynamic properties of brine film. **(c)** A snapshot of a reference system for studying the isolated rock-brine and unconfined brine-oil interfaces. The brine film is ~4 nm thick so that the brine-rock and brine-oil interfaces do not affect each other. Water is shown as blue (oxygen) and white (hydrogen) spheres. Oil (*n*-decane) is shown as cyan (carbon) and white (hydrogen) spheres. Na^+ and Cl^- ions are shown as orange and green spheres respectively. Rock is made of α-quartz and shown using a bar-and-stick model.

In addition to the setup in Fig. 1a, thin brine film systems without an explicit brine reservoir (see Fig. 1b) are also studied. After the system that is shown in Fig. 1a reaches an equilibrium, its middle portion (delineated using a red dashed box) is extracted to build the system that is shown in Fig. 1b. The chemical potential of the brine film in the new system is the same as that in the original system, which features an explicit brine reservoir; however, the dimension (and, thus, the computational cost) of the new system is smaller. Systems that are set up this way are used to study the hydrodynamic properties of thin brine films.

The second type of system, namely, the "*thin water film*" system, is similar to the *thin brine film* system except that the quartz surface is neutral and there are no ions in the system. This type of system is used to study the hydration force in thin water films in the absence of any surface

charge or salinity effects. The third type of system is the "*reference"* system. In this type of system, a thick brine slab (~4 nm thick) is sandwiched between a thick oil slab (~4 nm thick) and the quartz slab (see Fig. 1c). Because bulk-like behavior occurs for the water and oil away from the rock-brine and brine-oil interfaces, the rock-brine and brine-oil interfaces do not affect each other substantially. Therefore, this type of system enables us to study the brine/EDLs near isolated rock surfaces and unconfined oil-brine interfaces, which are useful references for investigating the behavior of thin brine films.

Table 1. *The parameters of the three types of systems.*

	Thin brine film	Thin water film	Reference
System snapshots	Fig. 1a, Fig. 1b	-	Fig. 1c
Brine (water) film thickness	0.7nm – 1.0nm	0.7nm – 1.0nm	~4.0nm
Oil slab thickness	~4.0nm	~4.0nm	~4.0nm
Salt concentration	0.1 M, 1 M	0	0, 0.1 M, 1 M
Quartz slab's surface charge density	-0.12 C/m^2	0	0, -0.12C/m^2
Box length in *x, y, z*-directions	14.00×3.93×18.00nm^3 5.50×3.93×10.00nm^3	14.00×3.93×18.00nm^3 5.50×3.93×10.00nm^3	5.50×3.93×13.00nm^3

For the first type of OBR systems, four systems with two brine film thicknesses and two brine concentrations are studied; for the second type, two systems with two brine film thickness are studied; and for the third type, two systems with bulk ion concentrations of 0.1 M and 1 M are studied. The brine film thickness, brine reservoir ion concentration, and other parameters of the three types of systems are summarized in Table 1.

Molecular models. Water is described using the rigid SPC/E model.[39] *n*-decane is modeled using the optimized parameter set of the original OPLS-AA force fields for hydrocarbons.[40] The force field parameters for Na^+ and Cl^- ions are obtained from Ref. 41. The rock is composed of α-quartz. The quartz slab that is shown in Fig. 1a measures ~11 nm and 3.93 nm in the *x*- and *y*-directions, respectively. Its upper and lower surfaces are cleaved from the (101) plane by following the recent study of the quartz-water interface,[42] thereby yielding a surface silanol group density of 5.92 per nm^2. This silanol group surface density leads to a strongly hydrophilic surface, as suggested by previous work,[43-44] which facilitates the formation of brine film on the quartz surface in OBR systems.[44-46] Following prior work,[42] the zero plane of the quartz slab is defined as the *z*-

position of the second-outermost layer of surface silicon atoms (see Fig. S1 in the Supporting Information). The outermost silanol groups of the quartz surface that faces the oil phase are selectively deprotonated via the method in Ref. 42 to produce a net surface charge density of -0.12 C/m^2. The force field parameters of the quartz thus prepared, which include the Lennard-Jones (LJ) parameters and partial charges, are obtained from the CLAYFF force fields.[42, 47] To reduce the computational cost, the silicon and oxygen atoms of the quartz slab are fixed and their nonelectrostatic interactions with each other are excluded. The hydrogen atoms of the surface silanol groups are allowed to move by considering their bonded interactions with other atoms in the quartz slab. The LJ parameters for the interactions between dissimilar atoms are obtained using the Lorentz−Berthelot combination rule. The LJ potentials, partial charges and bonded parameters of atoms in the systems that are studied here are listed in the Supporting Information.

Simulation methods and protocol. All simulations are performed using the Gromacs code (version 4.5.6).[48] The bond lengths and angles of water molecules are constrained using the SETTLE algorithm. All simulations are conducted in the NVT ensemble with a temperature of 350K, which accords with typical reservoir conditions.[49-50] The temperature is maintained using the velocity rescale thermostat[51] with a time constant of 1 ps. A global cutoff of 1.2 nm is used to compute the LJ potentials and the particle mesh Ewald method with a slab correction to remove the periodicity in the *z*-direction is used to calculate the electrostatic interactions.[52]

The first type of systems with explicit brine reservoirs (see Fig. 1a) are built and equilibrated in four stages: In the first stage, an ~3-nm-thick brine slab is initially enclosed between the quartz surface and the oil slab. The top piston is allowed to move in the *z*-direction without applying any external force to it and the system is equilibrated for 4 ns. In the second stage, a 20 MPa pressure is exerted on the top piston to push the oil and brine downward to form a thin brine film between the oil and the quartz surface. During this stage, the thickness of the brine film in the middle portion of the system is recorded. Once the film thickness has reached 0.9 or 0.7 nm, the piston is fixed in space. In the third stage, the system is equilibrated further with the piston fixed. The pressure on the top piston and the numbers of ions and water molecules in the middle portion of the brine film (denoted by the red dashed box in Fig. 1a) are monitored over time. Typically, the pressure and the numbers of water molecules and ions in the brine film reach their equilibrium values within 200-500 ns (see Fig. S2 and Fig. S3 in the Supporting Information). In the final stage, the system

is simulated for another 100 ns to gather statistics. The equilibrium thickness of brine films that are built using this protocol is not prescribed *a priori* and typically differs from the film thickness at the end of the second stage. Via trial and error, the thickness of the equilibrated film has been adjusted to within 0.02 nm of the target values.

The first type of system without explicit brine reservoirs (see Fig. 1b) is built based on the brine film composition that was obtained at the end of the third stage. Once built, it is equilibrated for 50 ns, followed by the shearing simulations that are described in Section 3.4. The second type of system is built and equilibrated via a similar approach as the first type of system. The third type of system is built by stacking thick oil and brine slabs and equilibrating the system for 100 ns.

3. Results and Discussion

3.1 Structures of Interfacial Water and Oil

We begin with the structures of the interfacial water and oil in thin brine films, with a focus on how these structures differ from those near unconfined water-oil interfaces and isolated water-rock interfaces. The results that are presented below are based on systems that feature brine reservoirs with an ion concentration of 0.1 M. Similar interfacial oil and water structures are observed for the 1 M brine concentration cases and are not shown.

Water-oil interfaces. Figure 2 shows the water and decane density profiles in/near two brine films. The thickness of these brine films, which is denoted as h, is difficult to define uniquely. Here, h is defined under the assumption that a brine film is confined between the quartz and oil surfaces. Because water molecules can access the space ~0.22 nm above the quartz slab's zero plane, the effective surface of the quartz slab can be assigned to z=0.22 nm (see Fig. 2a). For decane, using the convention of assigning the positions of diffusive interfaces, its nominal surface is taken as the position where its density is 50% of the bulk density. With the above definition, the thicknesses of the brine films that are shown in Fig. 2a and 2b are determined as 0.74 and 0.94 nm, respectively. The Gibbs dividing surface can also be used to define the film thickness; however, since the above choice of film thickness definition is simple and widely used and our analysis and conclusion do not depend sensitively on the definition of the film thickness, the above definition of the film thickness is adopted throughout the text. The space below (above) the nominal decane surface is shaded in blue (green) to reflect that this space is occupied predominately by brine (oil).

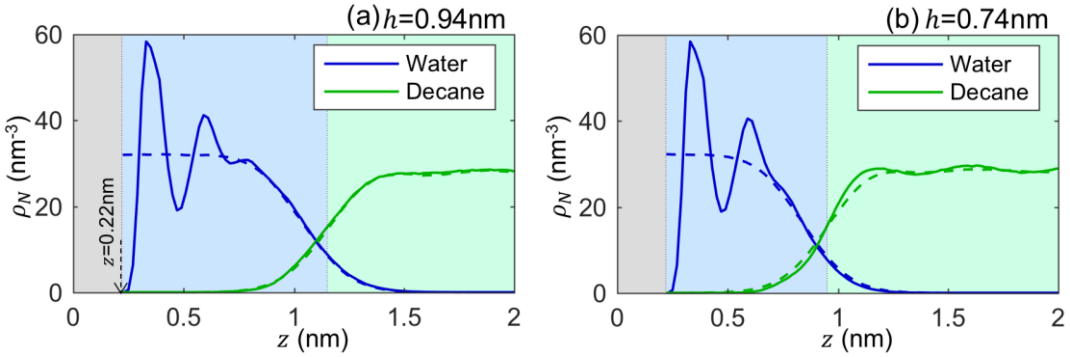

Figure 2. *Water-oil interface in brine films.* **(a-b)** The density profiles of water and oil in brine films with thicknesses of 0.94 nm (a) and 0.74 nm (b). The water density is calculated based on its center-of-mass position and the oil density is calculated from the number density of carbon atoms. The areas that are shaded in blue and green correspond to the water and oil phases, which are separated by a plane at which the decane density is half of its bulk value. The dashed lines represent the reference density profiles of interfacial water (in blue) and decane (in green) near unconfined brine-oil interfaces. The reference density profiles are placed such that the water-oil phase boundary meets.

Figure 2a shows that when the brine film is 0.94 nm thick, the density profiles of water and decane near the water-oil interface are almost identical to those near unconfined interfaces. As the film is thinned to 0.74 nm, the density profile of water that is very close to the water-oil interface remains little changed; however, that of the oil becomes slightly sharper (see Fig. 2b). Hence, the oil surface that bounds a brine film becomes sharper (more well-defined) when film is thinned to ~2-3 layers of water molecules. Sharper oil surfaces are also observed in brine films with a bulk ion concentration of 1 M (see Fig. S4 in the Supporting Information).

Structure of interfacial oil. The sharpening of the oil surface above thinner brine films occurs because as a brine film becomes thinner, the oil molecules above it maintain a similar conformation but assume a more parallel alignment with respect to the brine-oil interfaces. To demonstrate this, we fit each decane molecule into an ellipsoid and determine its three principal axes $\boldsymbol{S}_k$ (k=1, 2, 3) and radius of gyration R_g (see Fig. 3c's inset and the Supporting Information). The orientation of the decane molecule at position z with respect to the oil-brine interface is characterized by the order parameter

$$\lambda_k(z) = \langle 3(\boldsymbol{S}_k(z) \cdot \boldsymbol{n_z})^2 - 1 \rangle / 2, \qquad (1)$$

where $\langle \cdot \rangle$ denotes the ensemble average and $\boldsymbol{n_z}$ is the unit normal vector of the oil-brine interface. $\lambda_k = 1$ (–0.5) if decane's k-th principal axis is normal (parallel) to the oil-brine interface.

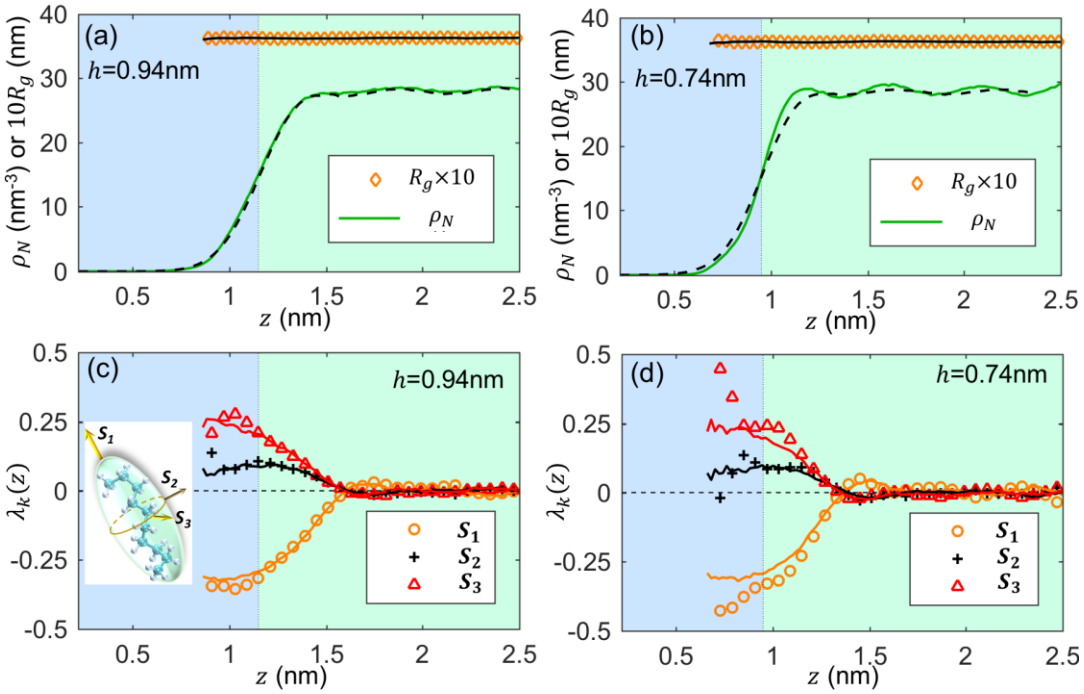

Figure 3. *Structure of oil near brine film-oil interfaces.* (**a-b**) The density and radius of gyration of decane near brine films with thicknesses of 0.94 nm (a) and 0.74 nm (b). Similar profiles near unconfined brine-oil interfaces are shown as black lines. (**c-d**) The orientation order parameter of the decane molecule's three principal axes near brine films with thicknesses of 0.94 nm (c) and 0.74 nm (d). Data for brine film-oil interfaces are shown as symbols, whereas those for unconfined brine-oil interfaces are shown as solid lines of the same color. The inset in (c) shows the three principal axes of a decane molecule.

Figure 3a and 3b show the radius of gyration of the decane molecules near brine-oil interfaces. We observe that R_g of decane molecules is maintained at 0.36 nm regardless of whether it is in bulk oil or at any position across water-oil interfaces; the latter has also been reported in prior work on interfacial hydrocarbon with similar chain length.[53] These results demonstrate that the conformation of a decane molecule that is in contact with the brine film changes little as the film is thinned.

Figure 3c and 3d show the order parameters of the principal axes of decane molecules near the brine-oil interfaces. As a decane molecule approaches an unbounded brine-oil interface, its longest axis becomes more parallel to the interface; hence, it tends to "lay" on the brine surface, similar to the phenomenon that was reported for linear alkanes near isolated water-oil interfaces.[5] When the brine film is 0.94 nm thick, the orientation ordering of the decane molecules near this film is nearly identical to that near unbounded brine-oil interfaces. As the film is thinned to 0.74 nm, λ_1 of the decane molecules that are in contact with the brine film decreases toward –0.5 while λ_3 increases toward 0.5, thereby suggesting that the interfacial decane molecules adopt a more parallel

orientation with respect to the brine surface. Because decane molecules that are in contact with the brine films are better aligned with the brine surface, these molecules tend to occupy a narrower space in the z-direction, thereby rendering the oil surface sharper. The more parallel orientation of interfacial decane above the 0.74-nm-thick brine film can be explained as follows: Many decane molecules that are directly above the 0.94-nm-thick film are in contact with water with a density that is close to that of bulk water (see Fig. 2a); many decane molecules above the 0.74-nm-thick film are in contact with the second water peak near quartz surfaces, which are packed more densely than bulk water (see Fig. 2b). Because it is more difficult to insert a decane molecule into more densely packed water, more decane molecules will "lay" on the surface of the 0.74-nm-thick brine film, thereby leading to a sharper oil surface. Furthermore, the more parallel orientation of the decane molecules near the thinner (0.74-nm-thick) brine film can also be explained by the solvation effects: When a decane molecule protrudes into a brine film, its molecular contact area with water increases and, as a result, a free energy cost is incurred. Near the thinner brine film, for the same increase of decane molecule-water contact area, the free energy cost is higher because the water molecules that solvate the protruding decane molecule are more densely packed originally (due to the layering of these water molecules near the quartz surface).

Water-rock interfaces. Figures 4a and 4b show the water density profiles near quartz surfaces that bound brine films with thicknesses of 0.94 and 0.74 nm, respectively. The density profile of water near an isolated quartz surface, which shows two distinct water layers that are centered at z=0.34 and 0.60 nm, as observed in previous works,[42] is also included in Fig. 4 as a reference. The water in the brine film can be divided into three layers according to the two valleys that are positioned at z_1=0.47 nm and z_2=0.71 nm (1st layer: $z_0 < z < z_1$; 2nd layer: $z_1 < z < z_2$; and 3rd layer: $z > z_2$). The water density in the third layer closely resembles that near the unconfined oil-water interfaces (see Fig. 2a and 2b). As brine films are thinned to 0.94 nm, the first two layers of water remain intact; only when the brine film is thinned to 0.74 nm does the second water layer become disturbed by the presence of water-oil interfaces nearby. The water-rock interface is hardly disturbed in the brine film down to approximately three water layers, which is a consequence of the strong interactions between water and the quartz surface: the first water layer interacts strongly with the surface silanol groups, whereas the second water layer mainly interacts with the densely packed water in the first layer. The soft, hydrophobic surface of oil impacts only the layer of water molecules that is in direct contact with it.

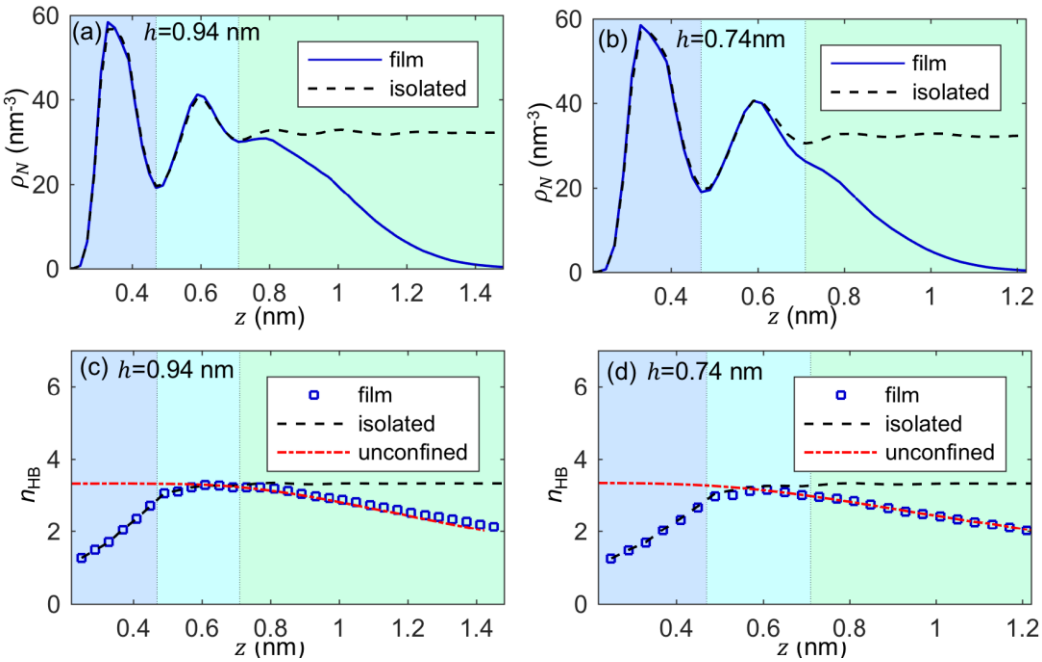

Figure 4. *Water-rock interface in brine films.* **(a-b)** The density profiles of water near an isolated quartz surface and across brine films with thicknesses of 0.94 nm (a) and 0.74 nm (b). The shaded areas denote the three water layers, which are separated by two valleys at z_1=*0.47* nm and z_2=*0.71* nm. **(c-d)** The hydrogen bond number profiles of water molecules in brine films with thicknesses of 0.94 nm (c) and 0.74 nm (d). The hydrogen bond profiles near unconfined interfaces are positioned similarly to the water/oil density profiles in Fig. 2.

The strong water-water/quartz interactions in the first two water layers near the quartz can be observed from the hydrogen bonds that are formed by the water molecules in brine films. Geometric criteria are used for hydrogen bonds[54]: a hydrogen bond exists if L_{oo}<0.35 nm and ∠OOH≤30° (L_{oo}: the oxygen-oxygen distance; ∠OOH: the angle that is formed between one water molecule's OH bond and the oxygen-oxygen vector that points from the donor to the acceptor). As shown in Fig. 4c and 4d, the number of hydrogen bonds per water molecule, which is denoted as n_{HB}, is smaller for water in the first layer than in the bulk due to their favorable interactions with surface silanol groups. n_{HB} is close to the bulk value in the second water layer; hence, dominant water-water interactions occur in this layer. Similar to the density profiles, the profiles of n_{HB} near the rock surface and the oil surface closely resemble those near the isolated quartz surface and the unconfined oil-water interface, respectively. As a side note, in both brine films, the orientations of their two layers of water molecules can deviate from those near isolated quartz surfaces (see Section 3.3).

The above results demonstrate that in brine films that are as narrow as 2-3 water layers, the packing of water molecules and the coordination between them can be reasonably approximated by those near isolated rock-brine interfaces and unconfined oil-brine interfaces. This differs from the water that is confined between two rigid surfaces, where the structure of water near one surface can be modified substantially when the two surfaces approach each other closely.[55]

3.2 Structure of Electrical Double Layers

In this part, we investigate the structure of EDLs in the thin brine films when the quartz slab has a surface charge density of σ=–0.12 C/m^2. The ion concentration in the brine reservoir is 0.1 M unless otherwise specified. We focus on the evolution of the ion distribution as the brine film thickness decreases and the underlying mechanisms.

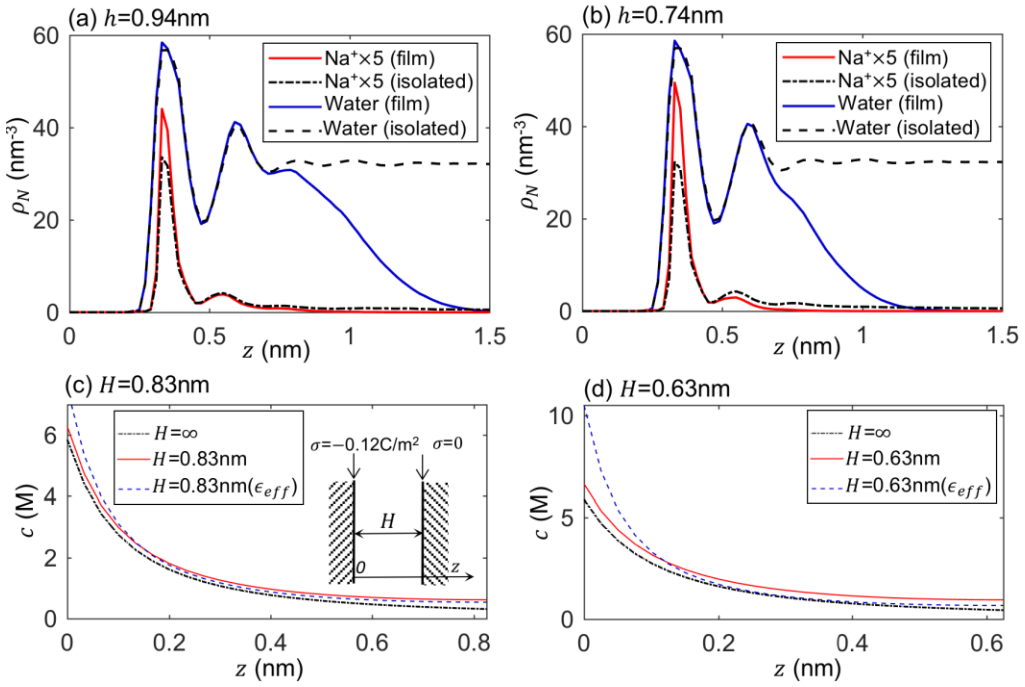

Figure 5. *Electrical double layers in thin brine films.* (**a-b**) The density profiles of Na^+ ions and water near an isolated quartz surface and in thin films with thicknesses of 0.94 nm (a) and 0.74 nm (b). (**c-d**) The Na^+ ion density that is predicted by the Poisson-Boltzmann equation in brine films with ion-accessible thicknesses of 0.83 nm (c) and 0.63 nm (d). The inset in (c) is the continuum model of the brine film. The ion-accessible thickness H is determined as the distance between the Na^+ ion's first peak and the nominal oil surface in (a-b). The brine film is in equilibrium with a brine reservoir with an ion concentration of 0.1 M. The co-ion density is not shown due to their very small values.

Ion distribution. Figure 5 shows the density profiles of Na^+ ions in two brine films and near isolated quartz surfaces. The average concentrations of Na^+ ions in the 0.74-nm-thick and 0.94-nm-thick brine films are 1.60 M and 1.24 M, respectively. The density profile of Cl^- ions is not shown because of their very small value, especially inside the brine films. Regardless of the brine film thickness (an isolated quartz surface is effectively bounded by a very thick brine film), two Na^+ density peaks appear at z=0.33 nm and 0.55 nm. The locations of these peaks are in excellent agreement with prior studies of EDLs near the same quartz surface.[42] As the brine film is thinned, the evolution of the Na^+ density profiles shows two features: First, the Na^+ density away from the quartz surface (e.g., at the second Na^+ peak) decreases substantially. For example, in the 0.74-nm-thick film, the height of the second Na^+ peak is reduced to 1/3 of its height near an isolated quartz surface. Second, the first Na^+ peak grows by 28.7% and 44.6% compared to that near isolated quartz surfaces as the film is thinned to 0.94 nm and, subsequently, to 0.74 nm.

The first feature and the existence of the second Na^+ peak are primarily caused by the ion hydration effect. In classic EDL theories such as the Poisson-Boltzmann (PB) equation, the ion distribution is governed by long-range ion-ion electrostatic interactions and water acts only as a dielectric medium. However, water also behaves as a molecular solvent that hydrates ions and the related short-range ion-water interactions have been found to substantially affect the ion distribution in EDLs.[56-61] To explore this effect, we compute the hydration number of Na^+ ions (n_{hdr}). n_{hdr} of an ion is defined as the number of water molecules within its first hydration shell. The radius of an ion's first hydration shell corresponds to the first minimum of the ion–water radial distribution function (RDF). For a Na^+ ion, the radius of its first hydration shell is approximately 0.31 nm (see Supporting Information). Calculation of n_{hdr} of Na^+ ions across the brine films revealed that n_{hdr} of Na^+ ions attains a local maximum at z=0.53 nm (see Fig. S7 in the Supporting Information), which is caused by the inhomogeneous distribution (layering) of water molecules near the quartz surface. Because a Na^+ ion is hydrated by more water molecules at this location than in bulk, it is energetically favorable to reside here, thereby helping explain the second Na^+ peak at z=0.55 nm. Similar solvent-induced effects have been reported in prior MD and DFT simulations of EDLs near solid surfaces.[56-61]

As a brine film is thinned, the oil surface moves toward the quartz surface. Since the water density is reduced near an oil surface, the ion hydration at a specified distance from the quartz

surface is reduced. For example, in the 0.74-nm-thick brine film, n_{hdr} of Na^+ ions in the region z>0.5 nm is substantially smaller than that in the 0.94-nm-thick brine films. Consequently, the Na^+ density in this region is lower than in the 0.94-nm-thick brine films.

The second feature of Na^+ density evolution, namely, the increase of the first Na^+ density peak as the brine films are thinned, can be caused by several factors. First, as brine films are thinned, Na^+ ions in the region away from the quartz surface are depleted as explained above. However, the number of Na^+ ions in the film remains almost unchanged because they must balance the charge on the quartz surface (the number of Cl^- ions in the brine film is negligible under the reservoir concentration that is studied here). Therefore, the Na^+ density close to the quartz surface will increase. Second, as the brine films are thinned, even if Na^+ ions are not repelled from the oil surface due to the hydration effect, these ions are confined in a narrower space; thus, the Na^+ density near the quartz surface should increase. Assessing whether the increased confinement in thinner brine films can lead to the higher first Na^+ peak is difficult because, ideally, this confinement effect should be evaluated using a model that incorporates all relevant physics (e.g., ion hydration effects) in addition to the geometrical confinement. While such models do exist, they often require empirical parameters as inputs.[62] Here, we use the classic PB equation to obtain a qualitative understanding only.

As shown in the inset of Fig. 5c, in the PB model, each brine film is represented as a slit pore that is bounded by one charged wall (which mimics the quartz surface) and one neutral wall (which mimics the neutral oil surface). Because the first Na^+ density peak at z=0.33 nm is 0.11 nm away from the nominal brine-quartz interface (see Fig. 5a and Fig. 2a), the width of the slit pore, which is denoted as H, is taken as 0.83 (0.63 nm) for the 0.94-nm-thick (0.74-nm-thick) brine film. The dielectric constant inside the pore, namely, ε_r, is set to 56.83±1.31, which is computed for bulk SPC/E water at 350 K (see the Supporting Information).[63-64] The ion concentration in the bulk electrolyte is set to 0.1 M, which is the same as that in our brine reservoir. As shown in Fig. 5c and 5d, the density of Na^+ ions on the pore increases by 7.4% and 12.9% as H decreases from ∞ to 0.83 nm and 0.74 nm, respectively. These increases are much smaller than the increases of the first Na^+ peak that are observed in Fig. 5a and 5b, thereby suggesting that the increased confinement in thinner brine films is likely not the direct reason for the increased Na^+ adsorption on the quartz surface.

Dielectric effects. In the above analysis, based on the PB equation, the dielectric constant of the brine film is taken as that of bulk water. However, the dielectric response of nanoconfined water is known to differ substantially from that in bulk,[65-67] which can modify electrostatic interactions between ions and, thus, affect the ion distribution in the brine film. To appreciate the dielectric effects in molecularly thin films, following the work of Netz and co-workers, we compute the dielectric profile of water in thin water films near neutral quartz surfaces.

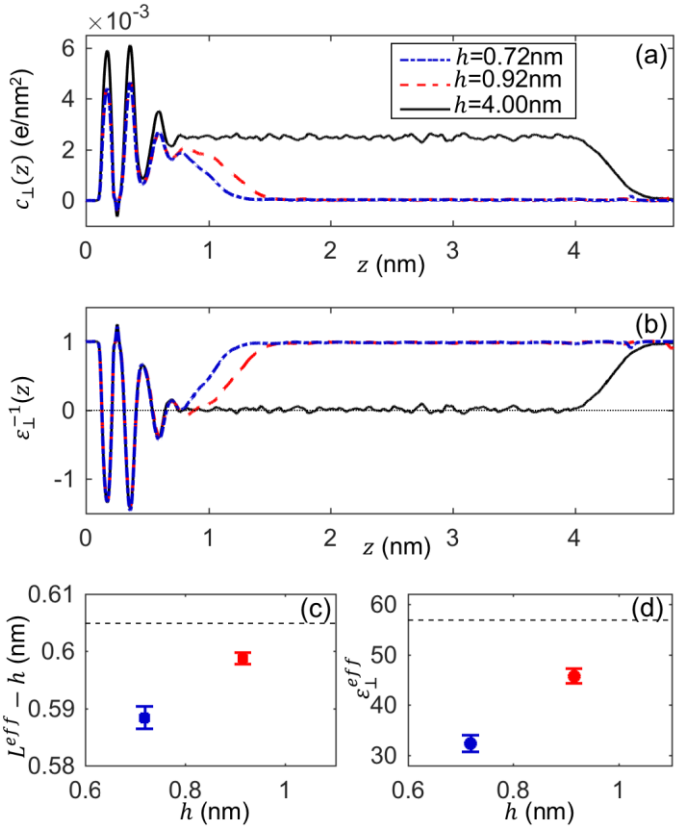

Figure 6. *Perpendicular dielectric profiles in thin water films.* **(a)** The polarization correlation function near the quartz surface. **(b)** The inverse perpendicular dielectric profile near the quartz surface. **(c)** The shift of the effective dielectric box length with respect to the film thickness. The dashed line denotes the shift when the water film is 4.0 nm thick. **(d)** The effective dielectric constant in the direction normal to the quartz surface. The dashed line denotes the static dielectric constant of bulk water.

The *thin water film* systems in Table 1 with film thicknesses of 0.72, 0.92, and 4 nm are studied. The component of the dielectric constant in the direction perpendicular to the quartz surface is of primary interest and is computed by following linear response theory.[66, 68-69] A perpendicular polarization correlation function is defined as

$$c_\perp(z) = \langle m_\perp(z) M_\perp \rangle - \langle m_\perp(z) \rangle \langle M_\perp \rangle \qquad (2)$$

where $\langle\cdot\rangle$ denotes the time average and $m_\perp(z)$ is the perpendicular polarization density at position z, which is evaluated via $m_\perp(z) = -\int_0^z \rho_e(z')dz'$ (ρ_e is the space charge density). The total perpendicular polarization of the simulation box is $M_\perp = L_x L_y \int_0^{L_z} m_\perp(z)dz$, where L_x, L_y, and L_z are the box lengths in the *x-, y-,* and *z*-directions. Using the fluctuation-dissipation theorem,[67-68] the inverse perpendicular dielectric profile of a periodic system is related to $c_\perp(z)$ via

$$\varepsilon_\perp^{-1}(z) = 1 - c_\perp(z)/(\varepsilon_0 k_B T + C_\perp/V), \quad (3)$$

where ε_0 is the vacuum permittivity, k_B is the Boltzmann constant, T=350K is the system temperature, $C_\perp = L_x L_y \int_0^{L_z} c_\perp(z)dz$ is the variance of the total polarization, and V is the simulation box volume. For sufficiently thick water films, $\varepsilon_\perp^{-1}(z)$ should approach $1/\varepsilon_r$ at positions that are away from the confining surfaces.

Figure 6a shows the perpendicular polarization correlation function in the studied water films. Near the quartz surface, whose zero plane is located at *z*=0, the $c_\perp(z)$ profiles of the two thin water films are undistinguishable from each other but are lower overall than that for the case with H=4 nm due to the larger value of $M_\perp$ for the much thicker water film. The corresponding $\varepsilon_\perp^{-1}(z)$ profiles are shown in Fig. 6b. Near the quartz surface, $\varepsilon_\perp^{-1}(z)$ crosses zero several times and exhibits negative values in some regions, namely, $\varepsilon_\perp(z)$ can become negative or diverge locally. Similar phenomena have been reported for water near many types of substrates and they correspond to the overscreening of surface charges at various positions by water.[66, 68-70] While it is not straightforward to evaluate how the complex $\varepsilon_\perp(z)$ affects dielectric screening in the water film, the complex $\varepsilon_\perp^{-1}(z)$ profile can be used to construct a coarse-grained dielectric box model that approximates the film as a continuum with a uniform effective dielectric constant.[66] According to linear response theory, such a dielectric box model effectively reproduces the integral over the electrical field by

$$\int_0^{L_z} (\varepsilon_\perp^{-1}(z) - 1)dz = L_\perp^{eff}(1/\varepsilon_\perp^{eff} - 1), \quad (4)$$

where $L_\perp^{eff}$ and $\varepsilon_\perp^{eff}$ are the effective dielectric box length in the *z*-direction and the effective perpendicular dielectric constant within the box, respectively. As for the original dielectric box model,[66] one computes $L_\perp^{eff}$ by setting $\varepsilon_\perp^{eff}$ to the dielectric constant of bulk water (56.83 here). Using the obtained value of $L_\perp^{eff}$, a shift $\delta = L_\perp^{eff} - h$ is obtained (h is the water film thickness). The effects of the quartz slab, oil phase, and water film on the dielectric profile are all lumped into the shift δ. Since the quartz slab and the oil phase are the same in systems with different water films,

the perpendicular dielectric profiles are the same in them (data not shown here). Therefore, δ in systems with different water film thicknesses h provides a measurement of how the dielectric environment is changed when h changes. Typically, δ varies monotonically as a water film becomes thicker and approaches an asymptotic value, namely, δ_0, when h is larger than a few nanometers. In thin films, it has been established that $\varepsilon_{\perp}^{eff}$ can be obtained via Eq. 4 and using the effective dielectric box length that is based on the asymptotic shift ($L_{\perp}^{eff} = h + \delta_0$).[66]

Figure 6c shows the shift δ in three water films. The shift δ for 4.0-nm-thick film is 0.715 nm. This value is taken as the asymptotic shift δ_0 and labeled using a dashed line. As the film thickness decreases to 0.92 and 0.72 nm, δ is reduced to 0.709 and 0.698 nm, respectively. The magnitude of δ for our water films, which are confined between a rigid quartz surface and a soft decane slab, is similar to that of the water films that are confined between two polar walls with similar separations.[66] δ decreases as a water film is thinned, which corresponds to a decrease of the dielectric efficiency of nanoconfined water in the direction normal to the confining surfaces. Furthermore, via the method that is described above, the effective dielectric constant $\varepsilon_{\perp}^{eff}$ is found to decrease to 57% and 81% of the bulk dielectric constant in films with h =0.72 and 0.92 nm, respectively (see Fig. 6d). Using these dielectric constants, the PB model that is sketched in Fig. 5c is solved again to evaluate how the Na^+ density in brine films changes as they are thinned. As shown in Fig. 5c and 5d, the new PB model predicts that as the film thickness decreases from $H = \infty$ to 0.94 and, subsequently, to 0.74 nm, the maximal Na^+ density in the film increases by ~30% and ~80%. The larger increases that are observed here are in better agreement with the increase of the first Na^+ peak that is predicted by the MD simulations than when the dielectric decrement in the thin films is neglected. Physically, as the effective dielectric constant in a film decreases, the Na^+-Na^+ and Na^+-surface electrostatic interactions become less screened, which leads to a stronger adsorption of Na^+ ions on the quartz surface.

Salinity effects. Finally, we examine the EDL structure in brine films in equilibrium with brine reservoirs with an ion concentration of 1.0 M. Figure S8 in the Supporting Information shows the counter-ion (Na^+) density profile across the film, along with the water density profiles (the co-ion density profiles are shown in Fig. S9 in the Supporting Information). The density of Na^+ ions is substantially reduced near the oil surface for the 0.90-nm-thick and 0.72-nm-thick brine films, which is again due to the reduced ion hydration near the oil surfaces, as explained above. In

contrast to the scenario in which the ion concentration in the reservoir is 0.1 M, the height of the first Na^+ peak near the quartz surface increases only ~10% as the brine film thickness decreases from $h = \infty$ to 0.90 and 0.72 nm, as expected. At a bulk ion concentration of 1.0 M, the Debye length is ~0.3 nm; thus, most of the charge on the quartz surface is screened by the Na^+ ions that are adsorbed on it (within the first Na^+ peak). Consequently, the height of the first Na^+ peak near the quartz surface is controlled mainly by the surface charge density and shows no substantial variation as the brine film is thinned.

3.3 Disjoining Pressure in Brine Films

The disjoining pressure in thin films is measured as the pressure difference between the top and bottom pistons in Fig. 1a. For films that are in contact with charged quartz substrates (σ=–0.12C/m^2), film thicknesses of 0.92 ± 0.02 nm and 0.72 ± 0.02 nm and brine reservoir ion concentrations of 0.1 M and 1 M are studied. Figure 7 shows the disjoining pressure of the films as functions of the film thickness at two ion concentrations. For brine films with a thickness of ~0.92 nm, the disjoining pressure increases from 2.45 to 3.57 MPa as the brine concentration decreases from 1 M to 0.1 M. A similar increase from 11.3 to 13.1 MPa is observed in brine films with a thickness of ~0.72 nm. The increased repulsion between the oil and quartz surfaces at lower salinity is consistent with the double-layer expansion mechanism for wettability alteration in OBR systems.[16, 71]

To interpret the above results more quantitatively, we observe that the total disjoining pressure Π is typically divided into the van der Waals component Π_{vdw}, the double-layer component Π_{edl}, and the hydration component Π_{hdr}. For the nanometer-thin films that are considered here, Π_{vdw} is typically much smaller than the other two components and, thus, is not discussed further. Directly measuring the individual components of Π in MD simulations is difficult. However, since Π_{hdr} and Π_{vdw} do not vary substantially within the salinity window that is studied here (0.1-1 M),[72-73] we use the measured change of Π in response to a salinity change to gain insight into the validity of classical theories in predicting Π_{edl} and its change with the salinity. Using the PB equation that is adopted in classic DLVO theory and the model of the brine film that is sketched in Fig. 5c, Π_{edl} can be obtained via the contact value theorem[1]

$$\Pi_{edl}(H) = k_B T\left(\sum_i \rho_i(z = H) - \sum_i \rho_{i,\infty}\right) \quad (5)$$

where $\rho_i(z = H)$ is number density of ion i on the neutral surface at $z = H$ in the inset of Fig. 5c, $\rho_{i,\infty}$ is the ion density in the brine reservoirs, and k_BT is the thermal energy. $\rho_i(z = H)$ can be obtained by solving the classical PB equation.

Solving Eq. 5 and the PB equation with a quartz surface charge density of –0.12 C/m^2, Π_{edl} in a 0.92±0.02-nm-thick brine film is determined as 1.26 and 0.02 MPa at brine concentrations of 0.1 and 1 M; in a 0.72±0.02-nm-thick brine film, Π_{edl} is 2.21 and 0.31 MPa at brine concentrations of 0.1 and 1 M. The increase of Π_{edl} at each brine film thickness that is due to the salinity reduction that is predicted by the PB equation agrees well with the MD results. This satisfactory agreement is fortuitous but not a coincidence. Indeed, the PB equation has also been shown to well predict Π_{edl} in nanometer-thick brine films that separate moderately charged soft surfaces.[62] The satisfactory performance of the PB equation originates from Π_{edl} in these films being dominated by the entropic effect that is associated with the enrichment of ions, which is captured by the PB equation.

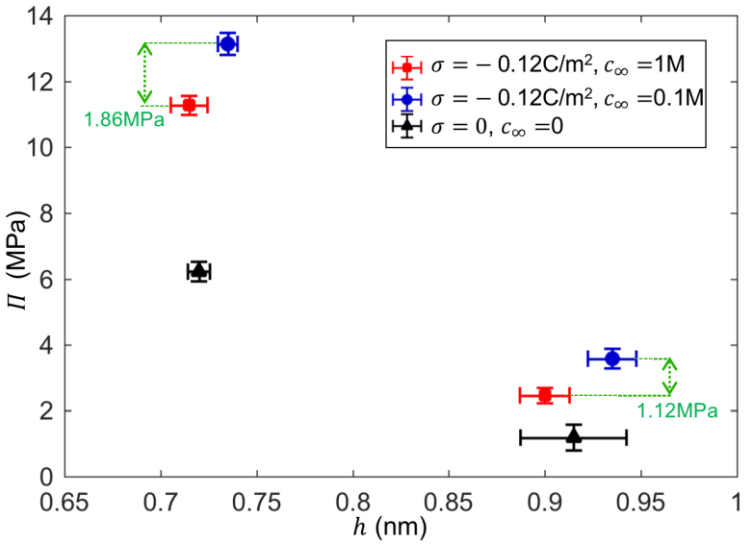

Figure 7. Disjoining pressures in thin films with various film thicknesses, quartz surface charge densities, and reservoir ion concentrations.

At a bulk ion concentration of 1 M, the observed value of Π should be mostly determined by Π_{hdr} because Π_{edl} is substantially suppressed according to the PB predictions. In many theoretical models of disjoining pressure, Π_{hdr} and Π_{edl} are assumed to be additive, namely, Π_{hdr} is assumed to be independent of Π_{edl} (and, hence, the surface charge and ion concentration). This additivity was shown to breakdown in thin films between rigid surfaces in early experiments[1] and in films between soft surfaces in recent MD simulations.[62] Here, we examine the extent to which Π_{hdr} in

thin films that separate a rigid quartz slab and a soft hydrocarbon liquid is affected by the quartz's surface charge. We studied the disjoining pressure in two water films (thicknesses: 0.72±0.02 and 0.92±0.02 nm) that are in contact with neutral quartz surfaces.

Figure 7 shows that when the quartz surface is neutral, the measured Π, which should be essentially Π_{hdr}, is 1.18 and 6.23 MPa in the 0.92-nm-thick and 0.72-nm-thick water films, respectively. In comparison, Π at 1 M ion concentration, which should also be dominated by Π_{hdr}, is 2.45 and 11.3 MPa in 0.90-nm-thick and 0.72-nm-thick brine films. These results demonstrate that Π_{hdr} increases as the quartz slab's surface charge density σ changes from 0 to –0.12 C/m^2 and, thus, it is not simply additive with Π_{edl}. The differences among the values of Π_{hdr} under various surface charge densities can be attributed to several factors: First, when σ changes from 0 to –0.12 C/m^2, many Na^+ ions become adsorbed on the quartz surface. The hydration of these Na^+ ions is stronger than that of the quartz surface because Na^+ ions are smaller than the silanol group. Therefore, water molecules are more difficult to remove near the charged quartz surface than near the neutral surface, thereby leading to a more repulsive Π_{hdr}. Second, when a quartz surface is electrified, the orientation of the interfacial water molecules and its evolution as the brine film is thinned, both of which affect the hydration force,[74-75] change, too. For example, the dipole orientation of water molecules near a neutral quartz surface changes little as a water film is thinned from $h = \infty$ to 0.92 nm (see Fig. S10a in the Supporting Information), whereas that near a charged quartz surface (σ=–0.12 C/m^2) changes substantially as a brine film is thinned from $h = \infty$ to 0.90 nm (see Fig. S10b in the Supporting Information). The larger change of the interfacial water molecules' orientation during the thinning of a brine film near a charged quartz surface helps explain the stronger Π_{hdr} in these films.

Overall, in films as thin as ~0.9 nm, the disjoining pressure is controlled by both the double-layer forces and the hydration forces; as films are thinned to ~0.7 nm, the hydration force dominates over the double layer force for ion concentrations as low as 0.1 M. However, the hydration force is not independent of the double-layer force in that it changes as the quartz surface becomes electrified. When the brine salinity is lowered, the response of the disjoining pressure can be predicted accurately by the classic PB equation. Hence, the hydration force is less dependent on the salinity than the surface charge density of the quartz surface in the films that are studied here.

3.4 Dynamics of Thin Brine Films

The oil-brine-rock interfaces are often subject to shearing in the lateral direction, e.g., when an oil slug moves through a pore under the action of a pressure gradient.[76-78] In available studies of such problems, the dynamic properties of brine films are taken as those of bulk brine and a no-slip boundary condition is assumed at the oil-brine interface due to the limited information on these aspects. In this section, we bridge this gap by studying the hydrodynamic properties of thin brine films. Without loss of generality, we focus on brine films with a reservoir concentration of 0.1 M.

First, we study the shearing of a reference system that features thick slabs of brine and oil (Fig. 1c). Here, the brine-rock and the brine-oil interfaces are isolated due to their large separation. Shearing is imposed by pulling the top piston in the x-direction with a constant speed of V_p (V_p is 70 m/s here; simulations with V_p=50 m/s showed the same hydrodynamic properties within statistical error). After a steady state has been reached, the velocities of water and decane are collected on the fly for 50 ns. Figure 8a and 8b show that away from the quartz-water and water-oil interfaces, the velocity profiles of water and decane are linear. The velocity of water is almost zero within the first water density peak (z<0.47 nm), which is consistent with the notion that water molecules are attracted strongly to the quartz surfaces.[79] Across the nominal brine-oil interface (z=4.07 nm), there is a velocity jump, which corresponds to a slip between the brine and oil phases. A similar interfacial slip has been identified in studies on weakly interacting fluids and was found to originate from the poor mixing of the two fluid phases across the diffuse fluid-fluid interface and/or the limited entanglement of molecular chains of the species from the two fluids.[80-82]

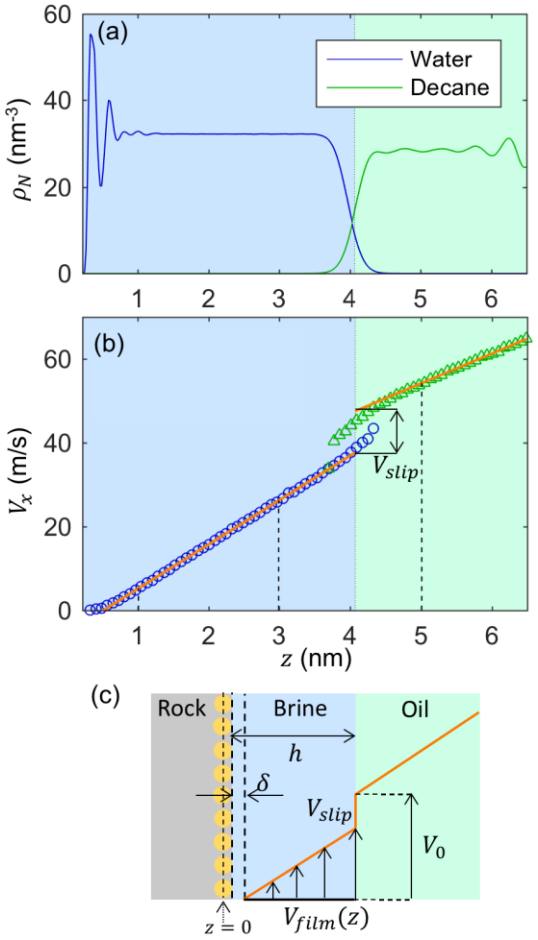

Figure 8. *Shear flow near quartz-brine and brine-oil interfaces.* **(a)** The number density profiles of water and decane's carbon atoms near the quartz surface in a *reference system* (see Fig. 1c). **(b)** The velocity profiles of water and decane. The shear flow is induced by pulling the top piston in Fig. 1c at a constant speed of 70m/s. **(c)** A schematic of the continuum model for describing the shearing flow in brine films.

In light of the above observations, we use a continuum model to describe the hydrodynamics of oil-brine-rock interfaces (see Fig. 8c). First, a no-slip plane is located at a distance δ from the brine-rock interface (the brine-rock interface is located 0.22 nm above the zero plane of the quartz surface; see Fig. 2a). Second, a slip occurs at the brine-oil interface with $V_{slip} = \tau/\beta$, where V_{slip} is the difference between the brine and oil velocities that are extrapolated from their profiles in their respective phases to the nominal brine-oil interface, β is the interfacial slip coefficient,[81, 83-84] and τ is the shear stress at the brine-oil interface. Finally, the Stokes equation with a constant effective viscosity ($\mu_{e,w}$ and $\mu_{e,d}$ for the brine and oil) is used to describe the flow in the brine and oil slabs. $\mu_{e,d}$ is taken as the bulk value of decane because the oil slab is thick. Using this model and the velocity profiles in MD simulations, δ, β, and $\mu_{e,w}$ can be obtained (see the Supporting Information). From the data that are presented in Fig. 8b, δ is determined as 0.29 nm and β is found

to be 0.39 ± 0.04 MPa·s/m. $\mu_{e,w}$ is determined to be 0.39 mPa·s, which is almost the same as that of bulk water.

Table 2. *Effective water viscosity and brine-oil slip coefficient for brine films**

Film thickness (h / nm)	0.94	0.94	0.74	0.74	4.00
Piston speed (m/s)	40	20	40	20	70
$\boldsymbol{\mu_{e,w}}$ (mPa·s)	0.40±0.05	0.37±0.02	0.33±0.03	0.32±0.01	0.39±0.04
$\boldsymbol{\beta}$ (MPa·s/m)	0.41±0.04	0.40±0.08	0.46±0.03	0.44±0.05	0.39±0.04

* the ion concentration in the brine reservoir is 0.1M.

Next, we simulated the shearing of oil-brine-rock interfaces in thin brine films. Figure S12a and S12b in the Supporting Information show velocity profiles in brine films with thicknesses of 0.74 and 0.94 nm, respectively. Their key features, namely, the shift of the no-slip boundary away from the quartz surface and the interfacial slip, are similar to those in Fig. 8b. The continuum model in Fig. 8c is also applied to these brine films with $\mu_{e,w}$ and β as adjustable parameters and $\mu_{e,d}$ taken as the bulk oil viscosity (0.63 mPa·s). The no-slip plane near the quartz surface is assumed to remain at the same position as in the reference system (z=0.51 nm or, equivalently, δ=0.29 nm) since water-rock interfaces in thin brine films differ little from those in the reference system (see Fig. 4). By requiring that V_{slip} at the brine-oil interface and the total water flux across the brine film that are predicted by the continuum model match those that are measured in MD simulations, $\mu_{e,w}$ and β in the brine films are extracted (see Table 2). The effectivity viscosities of water in the two brine films are the same as that of bulk water within statistical uncertainty. While the friction coefficient β at the brine-oil interfaces seems to increase marginally as a brine film is thinned, the variations are within the statistical error of our simulations. These results suggest that the hydrodynamic properties of brine films are not strongly affected by the molecular confinement in these films, which is consistent with the insensitivity of the structure of water in brine films and brine-oil interfaces to the brine film thickness (see Section 3.1).

For oil slugs inside a pore, the brine films between the slug and pore walls act like a slip layer, thereby facilitating the transport of the oil slug due to their lower viscosity than oil.[85] For a brine film with a thickness h and under a shear stress τ, the velocity of the oil at the brine-oil interface is $V_0/\tau = h/\mu_b$ according to the classic hydrodynamic models (μ_b is the viscosity of bulk water). In

light of the continuum model that is sketched in Fig. 8c, the velocity of the oil at the interface becomes $V_0'/\tau = (h-\delta)\mu_{e,w}^{-1} + \beta^{-1}$ or

$$V_0'/V_0 = \left(1-\frac{\delta}{h}\right)\mu_b\mu_{e,w}^{-1} + \mu_b/(\beta h). \quad (6)$$

The first term on the right-hand side accounts for the effects of the shifted shear plane from quartz surfaces and the deviations of the viscosities from their bulk values. The second term on the right-hand side accounts for the slip at brine-oil interfaces. For the 0.74- and 0.94-nm-thick films that are considered here, the first term is ~0.75-0.85 based on the data in Table 2, thereby suggesting that these effects only change the transport of oil slugs marginally. The second term is ~1 for the two films that are considered here, namely, due to the interfacial slip, the oil surface can move ~100% faster than when this slip is neglected. Physically, in terms of providing lubrication for the movement of an oil slug along a pore, the slip at the brine-oil interface effectively increases the apparent thickness of the brine layer between the oil slug and pore walls by $\ell = \mu_b/\beta$. If ℓ is comparable to the physical thickness h of the brine film, the interfacial slip substantially affects the transport of the oil slug. Because brine films in OBR systems are often thinner than one or a few nanometers,[18-19] the interfacial slip should be considered in future continuum simulations of oil droplet transport in OBR systems.

4. Conclusions

In summary, we studied molecularly thin brine films that are confined between nonpolar oil and quartz surfaces via MD simulations. We quantify the structures of the interfacial water, oil, and EDLs, the disjoining pressure, and the shearing properties of the brine films and brine-oil interfaces. The subnanometer confinement in brine films only weakly modifies the molecular packing at the rock-brine and brine-oil interfaces. However, increasing the confinement (thinning the brine films) markedly increases the counterion density near the charged quartz surfaces, especially under low brine concentration conditions. Although the increased geometrical confinement contributes *directly* to the enhanced counterion adsorption, its *indirect* contributions are more important, e.g., as the confinement is increased, the dielectric screening in brine films is weakened. The disjoining pressure in the films is dominated by the hydration forces. Interestingly, the disjoining pressure increases as the brine concentration is lowered and the magnitude of its increase is consistent with that predicted by the PB equation. An analysis of the disjoining pressure in systems with neutral and charged quartz surfaces demonstrates that the hydration disjoining

pressure increases substantially as the quartz surface is electrified. Hence, the hydration and double-layer forces are not simply additive, which is consistent with prior experimental measurements between solid surfaces and simulations of surface forces between soft surfaces.[1, 62] The first layer of water molecules on the quartz surface is effectively stagnant; however, the viscosity of water beyond this layer is bulk-like in brine films that are as thin as three water molecule layers. An interfacial slip is observed between the brine and oil phases, which contributes to an effective slip length of $\ell \sim 1$ nm in the systems that are investigated here.

The present study is based on simulations and a direct validation of its results is limited by the scarce experimental studies on OBR systems. We hope the results that are presented here will stimulate experimental investigations of thin brine films in the future. Nevertheless, insights from this study should help improve the fundamental understanding, numerical modeling, and application of technologies, including LSW. The little-disturbed structure and dynamic properties of interfacial water and oil as the brine films are thinned highlight that the water-rock and water-oil interfaces can be predicted reasonably well from unconfined water-rock and water-oil interfaces. The classical PB equation well predicts the responses of the disjoining pressure to salinity changes for the cases that are studied here. However, hydration forces not likely being additive with the double-layer force suggests that the classic surface force theories should be used with caution in modeling the disjoining pressure in brine films in OBR systems. Furthermore, the significant modification of the EDL structure and the decrease of the effective dielectric constant as the brine films are thinned will likely affect processes such as surface charge regulation.[86] Therefore, although these factors do not substantially change the disjoining pressure under the fixed surface charge condition that is explored here, they may play an important role in practice. Finally, the slip at brine-oil interfaces can substantially facilitate the transport of oil slugs in narrow pores by *effectively* providing a thicker slip layer for such transport.

Supporting Information available: Force fields parameters; Relaxation of thin brine films within the last 100ns; Structure of water-oil interfaces at 1M brine concentration; Quantification of the geometry of decane molecules; Na^+ ion hydration number profile across brine films, Static dielectric constant of SPC/E water; Radial distribution functions in NaCl solutions; Na^+ ion density profiles across brine films in equilibrium with 1M brine reservoirs ; Cl^- ion density profiles across brine films in equilibrium with 1M brine reservoirs; Water dipole orientation profiles; The

hydrodynamic properties of thick water film in Fig. 8; Shear flow velocity profiles in thin brine films.

Acknowledgements

We thank the ARC at Virginia Tech for generous allocations of computer time. The financial support from NSF under grant number CBET 1705287 is gratefully acknowledged.

References

1. Israelachvili, J. N., *Intermolecular and surface forces*. Academic press: 2011.
2. Lyklema, J., *Fundamentals of Interface and Colloid Science*. Academic press: 1995; Vol. II: Solid-Liquid Interfaces.
3. Bazant, M. Z.; Kilic, M. S.; Storey, B. D.; Ajdari, A., Towards an understanding of induced-charge electrokinetics at large applied voltages in concentrated solutions. *Advances in Colloid and Interface Science* **2009,** *152* (1), 48-88.
4. Zhan, C.; Lian, C.; Zhang, Y.; Thompson, M. W.; Xie, Y.; Wu, J.; Kent, P. R. C.; Cummings, P. T.; Jiang, D.-e.; Wesolowski, D. J., Computational Insights into Materials and Interfaces for Capacitive Energy Storage. *Advanced Science* **2017,** *4* (7), 1700059.
5. Fukuto, M.; Ocko, B.; Bonthuis, D. J.; Netz, R.; Steinrück, H.-G.; Pontoni, D.; Kuzmenko, I.; Haddad, J.; Deutsch, M., Nanoscale structure of the oil-water interface. *Physical review letters* **2016,** *117* (25), 256102.
6. Mamatkulov, S. I.; Khabibullaev, P. K.; Netz, R. R., Water at hydrophobic substrates: Curvature, pressure, and temperature effects. *Langmuir* **2004,** *20* (11), 4756-4763.
7. Janecek, J.; Netz, R. R., Interfacial water at hydrophobic and hydrophilic surfaces: Depletion versus adsorption. *Langmuir* **2007,** *23* (16), 8417-8429.
8. Sendner, C.; Horinek, D.; Bocquet, L.; Netz, R. R., Interfacial Water at Hydrophobic and Hydrophilic Surfaces: Slip, Viscosity, and Diffusion. *Langmuir* **2009,** *25* (18), 10768-10781.
9. Jiang, D.-e.; Jin, Z.; Wu, J., Oscillation of Capacitance inside Nanopores. *Nano Letters* **2011,** *11* (12), 5373-5377.
10. Sharma, A., Relationship of thin film stability and morphology to macroscopic parameters of wetting in the apolar and polar systems. *Langmuir* **1993,** *9* (3), 861-869.
11. Diao, Y. J.; Han, M. W.; Lopez-Berganza, J. A.; Valentino, L.; Marinas, B.; Espinosa-Marzal, R. M., Reconciling DLVO and non-DLVO Forces and Their Implications for Ion Rejection by a Polyamide Membrane. *Langmuir* **2017,** *33* (36), 8982-8992.
12. Han, M.; Espinosa-Marzal, R. M., Electroviscous Retardation of the Squeeze-Out of Nanoconfined Ionic Liquids. *The Journal of Physical Chemistry C* **2018**.
13. Qiu, Y. H.; Ma, J.; Chen, Y. F., Ionic Behavior in Highly Concentrated Aqueous Solutions Nanoconfined between Discretely Charged Silicon Surfaces. *Langmuir* **2016,** *32* (19), 4806-4814.
14. McEldrew, M.; Goodwin, Z. A. H.; Kornyshev, A. A.; Bazant, M. Z., Theory of the Double Layer in Water-in-Salt Electrolytes. *The Journal of Physical Chemistry Letters, DOI:10.1021/acs.jpclett.8b02543* **2018**.
15. Bazant, M. Z.; Storey, B. D.; Kornyshev, A. A., Double Layer in Ionic Liquids: Overscreening versus Crowding. *Physical Review Letters* **2011,** *106* (4), 046102.

16. Myint, P. C.; Firoozabadi, A., Thin liquid films in improved oil recovery from low-salinity brine. *Current Opinion in Colloid & Interface Science* **2015,** *20* (2), 105-114.
17. Morrow, N. R., *Interfacial Phenomena in Petroleum Recovery*. Marcel Dekker Inc.: New York, 1990.
18. Tokunaga, T. K., DLVO-Based Estimates of Adsorbed Water Film Thicknesses in Geologic CO2 Reservoirs. *Langmuir* **2012,** *28* (21), 8001-8009.
19. Lee, S. Y.; Webb, K. J.; Collins, I.; Lager, A.; Clarke, S.; apos; Sullivan, M.; Routh, A.; Wang, X., Low Salinity Oil Recovery: Increasing Understanding of the Underlying Mechanisms. In *SPE Improved Oil Recovery Symposium*, Society of Petroleum Engineers: Tulsa, Oklahoma, USA, 2010; p 11.
20. Bartels, W. B.; Mahani, H.; Berg, S.; Hassanizadeh, S. M., Literature review of low salinity waterflooding from a length and time scale perspective. *Fuel* **2019,** *236*, 338-353.
21. Tian, H.; Wang, M., Electrokinetic mechanism of wettability alternation at oil-water-rock interface. *Surface Science Reports* **2017,** *72* (6), 369-391.
22. Ding, H.; Rahman, S., Experimental and theoretical study of wettability alteration during low salinity water flooding-an state of the art review. *Colloids and Surfaces A: Physicochemical and Engineering Aspects* **2017,** *520*, 622-639.
23. Jackson, M. D.; Vinogradov, J.; Hamon, G.; Chamerois, M., Evidence, mechanisms and improved understanding of controlled salinity waterflooding part 1: Sandstones. *Fuel* **2016,** *185*, 772-793.
24. Al-Shalabi, E. W.; Sepehrnoori, K., A comprehensive review of low salinity/engineered water injections and their applications in sandstone and carbonate rocks. *Journal of Petroleum Science and Engineering* **2016,** *139*, 137-161.
25. Sheng, J. J., Critical review of low-salinity waterflooding. *Journal of Petroleum Science and Engineering* **2014,** *120*, 216-224.
26. Ayirala, S. C.; Al-Enezi, S. M.; Al-Yousef, A. A., A state of the art review to develop novel workflow for microscopic scale understanding of advanced water flooding mechanisms in carbonates. *Journal of Petroleum Science and Engineering* **2017,** *157*, 530-546.
27. Ayirala, S. C.; Yousef, A. A., A State-of-the-Art Review To Develop Injection-Water-Chemistry Requirement Guidelines for IOR/EOR Projects. *Spe Production & Operations* **2015,** *30* (1), 26-42.
28. Joekar-Niasar, V.; Mahani, H., Nonmonotonic Pressure Field Induced by Ionic Diffusion in Charged Thin Films. *Industrial & Engineering Chemistry Research* **2016,** *55* (21), 6227-6235.
29. Mahani, H.; Berg, S.; Ilic, D.; Bartels, W.-B.; Joekar-Niasar, V., Kinetics of Low-Salinity-Flooding Effect. *SPE-165255-PA* **2015,** *20* (01), 8-20.
30. Jiménez-Ángeles, F.; Firoozabadi, A., Tunable Substrate Wettability by Thin Water Layer. *The Journal of Physical Chemistry C* **2016,** *120* (43), 24688-24696.
31. Jiménez-Ángeles, F.; Firoozabadi, A., Contact Angle, Liquid Film, and Liquid–Liquid and Liquid–Solid Interfaces in Model Oil–Brine–Substrate Systems. *The Journal of Physical Chemistry C* **2016,** *120* (22), 11910-11917.
32. Koleini, M. M.; Badizad, M. H.; Kargozarfard, Z.; Ayatollahi, S., The impact of salinity on ionic characteristics of thin brine film wetting carbonate minerals: An atomistic insight. *Colloids and Surfaces A: Physicochemical and Engineering Aspects* **2019,** *571*, 27-35.
33. Tian, H. H.; Wang, M. R., Molecular dynamics for ion-tuned wettability in oil/brine/rock systems. *Aip Advances* **2017,** *7* (12).

34. Xu, S.; Wang, J.; Wu, J.; Liu, Q.; Sun, C.; Bai, B., Oil Contact Angles in a Water-Decane-Silicon Dioxide System: Effects of Surface Charge. *Nanoscale Research Letters* **2018,** *13* (1), 108.
35. Zheng, W.; Sun, C.; Wen, B.; Bai, B., Moving mechanisms of the three-phase contact line in a water–decane–silica system. *RSC Advances* **2019,** *9* (6), 3092-3101.
36. Zhao, J.; Yao, G.; Ramisetti, S. B.; Hammond, R. B.; Wen, D., Molecular dynamics investigation of substrate wettability alteration and oil transport in a calcite nanopore. *Fuel* **2019,** *239*, 1149-1161.
37. Uematsu, Y.; Bonthuis, D. J.; Netz, R. R., Impurity effects at hydrophobic surfaces. *Current Opinion in Electrochemistry* **2018**.
38. Lee, S. Y.; Webb, K. J.; Collins, I.; Lager, A.; Clarke, S.; O'Sullivan, M.; Routh, A.; Wang, X. In *Low salinity oil recovery: increasing understanding of the underlying mechanisms*, SPE improved oil recovery symposium, Society of Petroleum Engineers: 2010.
39. Berendsen, H.; Grigera, J.; Straatsma, T., The missing term in effective pair potentials. *Journal of Physical Chemistry* **1987,** *91* (24), 6269-6271.
40. Siu, S. W.; Pluhackova, K.; Böckmann, R. A., Optimization of the OPLS-AA force field for long hydrocarbons. *J. Chem. Theory Comput.* **2012,** *8* (4), 1459-1470.
41. Joung, I. S.; Cheatham III, T. E., Determination of alkali and halide monovalent ion parameters for use in explicitly solvated biomolecular simulations. *The journal of physical chemistry B* **2008,** *112* (30), 9020-9041.
42. Kroutil, O.; Chval, Z.; Skelton, A.; Predota, M., Computer simulations of quartz (101)–water interface over a range of pH values. *The Journal of Physical Chemistry C* **2015,** *119* (17), 9274-9286.
43. Emami, F. S.; Puddu, V.; Berry, R. J.; Varshney, V.; Patwardhan, S. V.; Perry, C. C.; Heinz, H., Force field and a surface model database for silica to simulate interfacial properties in atomic resolution. *Chemistry of Materials* **2014,** *26* (8), 2647-2658.
44. Fang, C.; Kang, Q.; Qiao, R., The Role of Disjoining Pressure and Thermal Activation in the Invasion of Droplets into Nanopores. *J. Phys. Chem. C* **2019**.
45. Khaneft, M.; Stühn, B.; Engstler, J.; Tempel, H.; Schneider, J. J.; Pirzer, T.; Hugel, T., Imbibition of polystyrene melts in aligned carbon nanotube arrays. *Journal of Applied Physics* **2013,** *113* (7), 074305.
46. Hu, J.; Ogletree, D.; Salmeron, M., The structure of molecularly thin films of water on mica in humid environments. *Surface science* **1995,** *344* (3), 221-236.
47. Cygan, R. T.; Liang, J.-J.; Kalinichev, A. G., Molecular models of hydroxide, oxyhydroxide, and clay phases and the development of a general force field. *The Journal of Physical Chemistry B* **2004,** *108* (4), 1255-1266.
48. Pronk, S.; Páll, S.; Schulz, R.; Larsson, P.; Bjelkmar, P.; Apostolov, R.; Shirts, M. R.; Smith, J. C.; Kasson, P. M.; Van Der Spoel, D., GROMACS 4.5: a high-throughput and highly parallel open source molecular simulation toolkit. *Bioinformatics* **2013,** *29* (7), 845-854.
49. Rexer, T. F.; Benham, M. J.; Aplin, A. C.; Thomas, K. M., Methane adsorption on shale under simulated geological temperature and pressure conditions. *Energy & Fuels* **2013,** *27* (6), 3099-3109.
50. Firoozabadi, A.; Ramey Jr, H. J., Surface tension of water-hydrocarbon systems at reservoir conditions. *Journal of Canadian Petroleum Technology* **1988,** *27* (03).

51. Bussi, G.; Donadio, D.; Parrinello, M., Canonical sampling through velocity rescaling. *J. Chem. Phys.* **2007,** *126* (1), 014101.
52. Darden, T.; York, D.; Pedersen, L., Particle mesh Ewald: An N· log (N) method for Ewald sums in large systems. *J. Chem. Phys.* **1993,** *98* (12), 10089-10092.
53. Murina, E. L.; Fernández-Prini, R.; Pastorino, C., Molecular conformation of linear alkane molecules: From gas phase to bulk water through the interface. *The Journal of chemical physics* **2017,** *147* (6), 064907.
54. Luzar, A.; Chandler, D., Hydrogen-bond kinetics in liquid water. *Nature* **1996,** *379* (6560), 55.
55. Allen, T.; Kuyucak, S.; Chung, S.-H., The effect of hydrophobic and hydrophilic channel walls on the structure and diffusion of water and ions. *J. Chem. Phys.* **1999,** *111* (17), 7985-7999.
56. Cui, S.; Cochran, H., Molecular dynamics simulation of interfacial electrolyte behaviors in nanoscale cylindrical pores. *The Journal of chemical physics* **2002,** *117* (12), 5850-5854.
57. Qiao, R.; Aluru, N., Atomistic simulation of KCl transport in charged silicon nanochannels: interfacial effects. *Colloids and Surfaces A: Physicochemical and Engineering Aspects* **2005,** *267* (1-3), 103-109.
58. Feng, G.; Qiao, R.; Huang, J.; Sumpter, B. G.; Meunier, V., Ion distribution in electrified micropores and its role in the anomalous enhancement of capacitance. *ACS nano* **2010,** *4* (4), 2382-2390.
59. Fleharty, M. E.; van Swol, F.; Petsev, D. N., Solvent Role in the Formation of Electric Double Layers with Surface Charge Regulation: A Bystander or a Key Participant? *Physical Review Letters* **2016,** *116* (4), 048301.
60. Vangara, R.; van Swol, F.; Petsev, D. N., Ionic solvation and solvent-solvent interaction effects on the charge and potential distributions in electric double layers. *The Journal of Chemical Physics* **2017,** *147* (21), 214704.
61. van Swol, F. B.; Petsev, D. N., Solution Structure Effects on the Properties of Electric Double Layers with Surface Charge Regulation Assessed by Density Functional Theory. *Langmuir* **2018,** *34* (46), 13808-13820.
62. Schlaich, A.; dos Santos, A. P.; Netz, R. R., Simulations of Nanoseparated Charged Surfaces Reveal Charge-Induced Water Reorientation and Nonadditivity of Hydration and Mean-Field Electrostatic Repulsion. *Langmuir* **2018,** *35* (2), 551-560.
63. Wasserman, E.; Wood, B.; Brodhol, J., The static dielectric constant of water at pressures up to 20 kbar and temperatures to 1273 K: Experiment, simulations, and empirical equations. *Geochimica et cosmochimica acta* **1995,** *59* (1), 1-6.
64. Gereben, O.; Pusztai, L., On the accurate calculation of the dielectric constant from molecular dynamics simulations: The case of SPC/E and SWM4-DP water. *Chemical Physics Letters* **2011,** *507* (1-3), 80-83.
65. Buyukdagli, S.; Blossey, R., Dipolar correlations in structured solvents under nanoconfinement. *The Journal of chemical physics* **2014,** *140* (23), 234903.
66. Schlaich, A.; Knapp, E. W.; Netz, R. R., Water dielectric effects in planar confinement. *Physical review letters* **2016,** *117* (4), 048001.
67. Ballenegger, V.; Hansen, J.-P., Dielectric permittivity profiles of confined polar fluids. *The Journal of chemical physics* **2005,** *122* (11), 114711.

68. Bonthuis, D. J.; Gekle, S.; Netz, R. R., Profile of the static permittivity tensor of water at interfaces: Consequences for capacitance, hydration interaction and ion adsorption. *Langmuir* **2012,** *28* (20), 7679-7694.
69. Bonthuis, D. J.; Gekle, S.; Netz, R. R., Dielectric profile of interfacial water and its effect on double-layer capacitance. *Physical review letters* **2011,** *107* (16), 166102.
70. Bopp, P. A.; Kornyshev, A. A.; Sutmann, G., Frequency and wave-vector dependent dielectric function of water: Collective modes and relaxation spectra. *The Journal of chemical physics* **1998,** *109* (5), 1939-1958.
71. Nasralla, R. A.; Nasr-El-Din, H. A., Double-layer expansion: is it a primary mechanism of improved oil recovery by low-salinity waterflooding? *SPE Reservoir Evaluation & Engineering* **2014,** *17* (01), 49-59.
72. Chapel, J. P., Electrolyte Species Dependent Hydration Forces between Silica Surfaces. *Langmuir* **1994,** *10* (11), 4237-4243.
73. Grabbe, A.; Horn, R. G., Double-Layer and Hydration Forces Measured between Silica Sheets Subjected to Various Surface Treatments. *Journal of Colloid and Interface Science* **1993,** *157* (2), 375-383.
74. Cevc, G.; Podgornik, R.; Zeks, B., The free energy, enthalpy and entropy of hydration of phospholipid bilayer membranes and their difference on the interfacial separation. *Chemical Physics Letters* **1982,** *91* (3), 193-196.
75. Kanduč, M.; Schlaich, A.; Schneck, E.; Netz, R. R., Hydration repulsion between membranes and polar surfaces: Simulation approaches versus continuum theories. *Advances in colloid and interface science* **2014,** *208*, 142-152.
76. Wilmott, Z.; Breward, C.; Chapman, S., The effect of ions on the motion of an oil slug through a charged capillary. *Journal of Fluid Mechanics* **2018,** *841*, 310-350.
77. Starov, V. M.; Kalinin, V. V.; Ivanov, V. I., Influence of surface forces on hydrodynamics of wetting. *Colloids and Surfaces A: Physicochemical and Engineering Aspects* **1994,** *91*, 149-154.
78. Kuchin, I.; Matar, O.; Craster, R.; Starov, V., Influence of the disjoining pressure on the equilibrium interfacial profile in transition zone between a thin film and a capillary meniscus. *Colloids and Interface Science Communications* **2014,** *1*, 18-22.
79. Thompson, P. A.; Robbins, M. O., Shear flow near solids: Epitaxial order and flow boundary conditions. *Physical review A* **1990,** *41* (12), 6830.
80. Barsky, S.; Robbins, M. O., Molecular dynamics study of slip at the interface between immiscible polymers. *Physical Review E* **2001,** *63* (2), 021801.
81. Koplik, J.; Banavar, J. R., Slip, immiscibility, and boundary conditions at the liquid-liquid interface. *Physical review letters* **2006,** *96* (4), 044505.
82. Razavi, S.; Koplik, J.; Kretzschmar, I., Molecular dynamics simulations: insight into molecular phenomena at interfaces. *Langmuir* **2014,** *30* (38), 11272-11283.
83. Zhao, R.; Macosko, C. W., Slip at polymer–polymer interfaces: Rheological measurements on coextruded multilayers. *Journal of rheology* **2002,** *46* (1), 145-167.
84. Schlaich, A.; Kappler, J.; Netz, R. R., Hydration friction in nanoconfinement: From bulk via interfacial to dry friction. *Nano letters* **2017,** *17* (10), 5969-5976.
85. Wilmott, Z. M.; Breward, C. J. W.; Chapman, S. J., Modelling Low-Salinity Oil Recovery Mechanisms Using an Ion Dissociation Model. *Transport in Porous Media* **2019,** *127* (3), 685-709.

86. Trefalt, G.; Behrens, S. H.; Borkovec, M., Charge Regulation in the Electrical Double Layer: Ion Adsorption and Surface Interactions. *Langmuir* **2016,** *32* (2), 380-400.

TOC Image

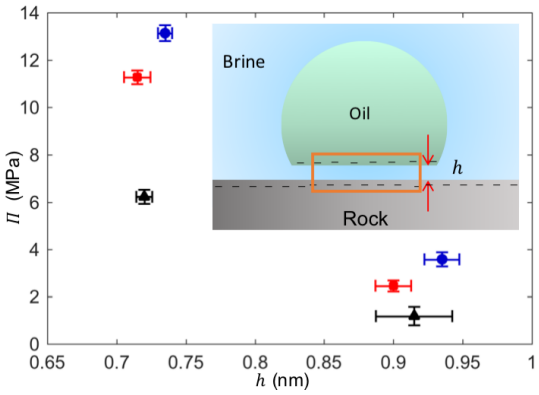
Brine
Oil
Rock
h
Π (MPa)
h (nm)
0
2
4
6
8
10
12
14
0.65
0.7
0.75
0.8
0.85
0.9
0.95
1